Exploiting localized transition waves to tune sound propagation in soft materials

Audrey A. Watkins, Austin Eichelberg, and Osama R. Bilal ●*

Department of Mechanical Engineering, University of Connecticut, Storrs, Connecticut 06269, USA

Programmable materials hold great potential for many applications such as deployable structures, soft robotics, and wave control; however, the presence of instability and disorder might hinder their utilization. Through a combination of analytical, numerical, and experimental analyses, we harness the interplay between instabilities, geometric frustration, and mechanical deformations to control the propagation of sound waves within self-assembled soft materials. We consider levitated magnetic disks confined by a magnetic boundary in-plane. The assemblies can be either ordered or disordered depending on the intrinsic disk symmetry. By applying an external load to the assembly, we observe the nucleation and propagation of different topological defects within the lattices. In the presence of instabilities, the defect propagation gives rise to *time-independent* localized transition waves. Surprisingly, in the presence of frustration, the applied load briefly introduces *deformation-induced order* to the material. By further deforming the lattices, new patterns emerge across all disk symmetries. We utilize these patterns to tune sound propagation through the material. Our findings could open new possibilities for designing exotic materials with potential applications ranging from sound control to soft robotics.

Patterns emerge within an assembly when the system elements are left to interact based on their individual energy [1]. When an external load is applied to these self-assembled patterns, the elements keep reorienting themselves to minimize their energy, resulting in different patterns [2]. In the case of incompatible elements, geometric frustration [3–6] can arise, particularly, when the global energy minima of the system is incompatible with the minima of the individual elements [7]. Such geometric frustration can prohibit the self-assembly from achieving long-range order. Furthermore, the presence of instabilities can influence the emerging order (or disorder) within a tunable material [8–14]. A valid path for functional tunability of matter is external stimuli (such as heat or magnetic fields) which can effectively apply an external load to tune material properties [15–20]. For soft materials, however, this usually translates to large deformation with the potential rise of instabilities, disorder, incompatibility, and geometric frustration. While such materials hold great potential for many applications such as deployable structures, soft robotics [21–23], and wave control [16,17,24–29], the presence of frustration, instability, and disorder within tunable soft materials might hinder their utilization. Here, we analytically, numerically, and experimentally show that in the presence of instabilities and disorder, pattern evolution due to deformation can be harnessed. By deforming our lattices, we control the nucleation and propagation of topological defects as time-independent localized transition waves. Furthermore, we exploit the evolving patterns to tune the propagation of sound waves within our material systems.

We consider the mechanics of levitated disks (lying in the horizontal plane) with repulsive magnetic interactions within a fixed magnetic boundary. The boundary magnets are equally spaced. The embedded disk magnets vary between 1 and 4, resembling the shape of a dot, line, triangle, and a square (Fig. 1). The boundary magnets create energy potential wells dictating the alignment of the free-floating disks. When confined within an energy potential well, a single disk translates and rotates freely to minimize its own energy. For a disk with one magnet, the minimum energy state is at the center of the energy potential well (i.e., the center of the four boundary magnets). In the case of two or four magnets per disk, the disk has four degenerate minimum energy states located at the center of the potential well with a 90° phase angle ϕ [Figs. 1(a)
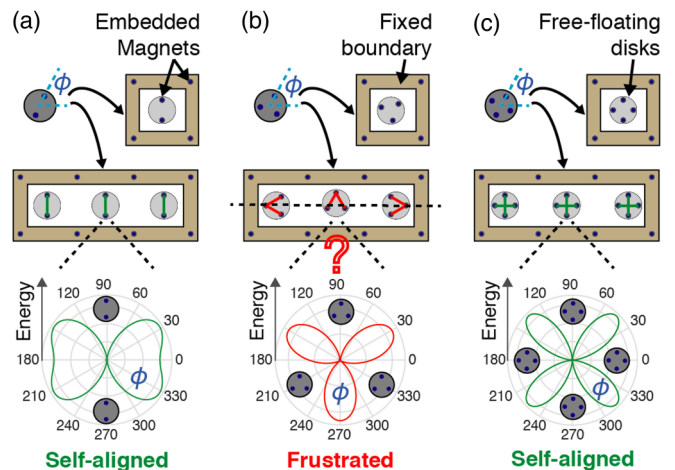

FIG. 1. *Concept.* Minimum energy state for one disk (top) and three disks (middle) confined by a fixed boundary with (a) two, (b) three, and (c) four magnets per disk. The potential energy as a function of the disk phase angle for the central disk is shown as a polar plot (bottom).

*osama.bilal@uconn.edu

and 1(c)]. In the case of three magnets per disk, there exist multiple minimum energy states that are off-center. Each of these off-center positions has three minimum energy states with a 120° phase angle [Fig. 1(b)]. When multiple disks are confined within the boundary, the self-alignment must take into account the added nearest-neighbor interaction. For both two and four magnets per disk, the minimum energy states exist at the center of the potential wells, resulting in perfectly aligned self-oriented lattices [Figs. 1(a) and 1(c), middle]. In the case of three magnets per disk, the disks have no clear state of self-alignment that minimizes both their individual and total energies, hence the system is *frustrated* [Fig. 1(c)]. To experimentally validate the potential energy calculations [Figs. 1(a)–1(c)], we enclose each disk type (i.e., with one to four magnets) within a fixed boundary atop an air bearing table. Both examples of the numerical and the experimental self-aligned disks with one to four embedded magnets are included in the Supplemental Material [30]. The disks start in random positions relative to the boundary and to each other. Then, we pressurize the air bearing, activating a layer of laminar air flow beneath the surface of the disks to allow them to float freely in the horizontal plane (i.e., levitating the disks similar to the arcade game "Air Hockey").

To study the wave propagation characteristics of the assemblies, we first consider a model of infinite periodic lattices with a single disk and its four boundary magnets as the unit cell with nearest-neighbor interaction (i.e., the immediately adjacent disks). Only the free-floating disks are allowed to move on both sides of the considered disk. Each disk has two degrees of freedom in the x and y directions. The dispersion relation of the system can be calculated using Bloch's theorem as $[-\omega^2 \mathbf{M} + \mathbf{K}(\kappa)]\boldsymbol{\phi} = 0$, where ω is the frequency, κ is the wave number, $\boldsymbol{\phi} = [u\ v]^T$ is the Bloch displacement vector in the x and y directions, $\boldsymbol{M}$ is the mass matrix, and $\boldsymbol{K}(\kappa)$ is the stiffness matrix [31], taking into consideration the static repulsive forces between the disks in the equilibrium configuration [32] (see Supplemental Material [30]). For disks with three embedded magnets, we assume perfect alignment of the disks in order to use Bloch's theorem. The analytically computed dispersion curves show two distinctive bands representing the longitudinal and shear motion in each of the four lattices [Figs. 2(a)–2(d)]. In addition, as the number of magnets per disk increases, the frequency of the bands increases, due to the increase in stiffness within the lattice.

To numerically verify the infinite model, we consider a finite arrangement of ten disks confined to a magnetic boundary (using the Verlet method [33]). The disks can move freely in-plane. The simulations are initialized with random disk positions. After the model reaches equilibrium, based on the balance of repulsive forces, we excite the rightmost disk with a chirp signal between 0.2 and 10 Hz. The fast Fourier transform (FFT) of the longitudinal transmission ranges matches closely with the analytical model [Figs. 2(e)–2(h)]. Remarkably, in the case of frustrated disks (i.e., with three magnets), the simulated transmission through the disordered lattice closely matches the dispersion curve calculated for a perfectly ordered lattice.

To experimentally verify the dispersion curves, we harmonically excite the longitudinal mode of the floating self-aligned lattices [Figs. 2(i)–2(l)] using a mechanical
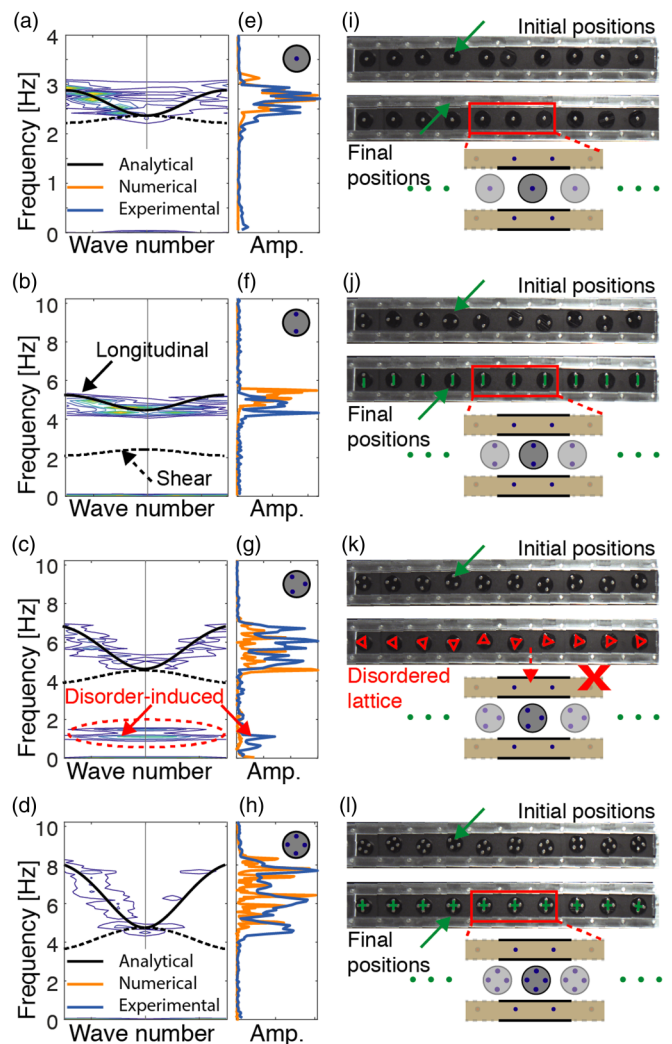

FIG. 2. *Lattice wave propagation.* (a)–(d) Analytical (black) and experimental (contour) dispersion curves for one to four magnets per disk. Numerical (orange) and experimental (blue) transmission at a central disk within the assembly. (i)–(l) The initial and final positions of ten disks with one to four embedded magnets. All the lattices are perfectly aligned except for three magnets per disk in panel (k).

shaker with a chirp signal between 0.2 and 10 Hz and measure the x displacement of the disks through digital image correlation. The longitudinal excitation takes place at the rightmost disk. The oscillatory motion of the disks is processed using one-dimensional (1D) and two-dimensional (2D) fast Fourier transform, resulting in a transmission spectrum and an experimental dispersion curve, respectively (see Supplemental Material [30]).

The experimentally measured transmission ranges (1D FFT) and dispersion curves (2D FFT) are in agreement with our numerical predictions within the longitudinal mode [Figs. 2(e)–2(h)]. Once more, in the presence of frustration, the experimentally measured transmission and dispersion through the disordered lattice matches closely with a perfectly ordered lattice. In addition, we note the emergence of an extra transmission band around 1 Hz for both measured transmission and dispersion. This transmission anomaly
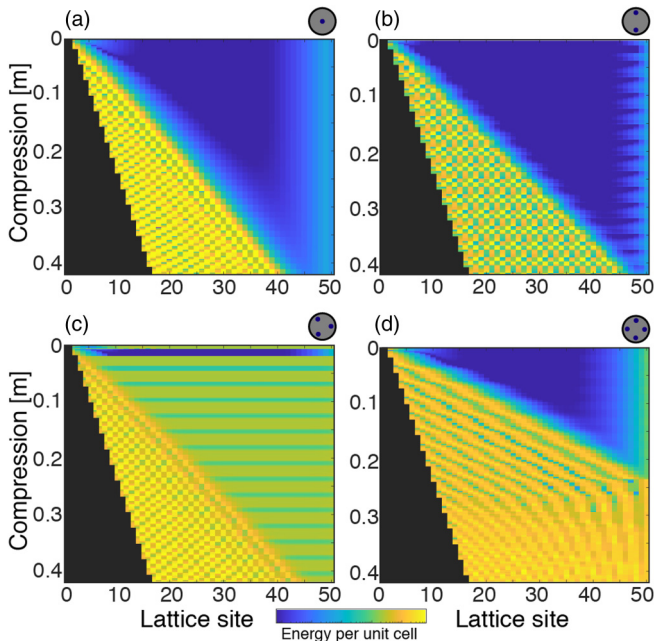
FIG. 3. *Time-independent transition wave*. Numerically obtained energy per unit cell as the lattice is compressed for (a) one, (b) two, (c) three, and (d) four embedded magnets per disk.

dissipates as the wave propagates further down the lattice due to the increased disorder. We note that there is no experimental transmission correlating with the shear modes, due to the absence of shear excitation.

A viable strategy for tuning wave propagation in soft material is applying an external load to tune stiffness [13,34–37]; however, this usually tunes the material globally. An intriguing feature of our material is the localized pattern transformation enabled by the boundary-induced multistability of the potential wells. When a load is applied at one end of the material, the disks initially experience an added global stiffness. Once the applied load passes a threshold, the first disk overcomes its boundary potential and snaps into the next potential well. As the compression at the boundary increases, the migration of disks between potentials creates a propagating defect, which gives rise to a stable transition wave. If the compression pauses, the propagation of the defects throughout the lattice stops (i.e., the transition wave is *time independent*).

We numerically simulate the compression of a 50-disk chain for each disk type using the Verlet method (Fig. 3). The disks start at random positions (and phase angle in cases of more than one magnet per disk) within their potential wells. After reaching equilibrium, we periodically increase the load applied at the leftmost disk with intermittent pauses allowing the disks to reassemble. In the case of one magnet per disk, the material starts at an equilibrium state with all disks experiencing the same repulsion forces, except those at the boundary [Fig. 3(a)]. As the load increases, the leftmost disk escapes its potential well, snaps into the next well, and consequently creates the first defect in the chain. This takes place once the disk overcomes the energy barrier formed by the vertical pair of boundary magnets. When the load increases further, the second disk snaps into the next potential well and the defect

propagates further down the chain as another defect nucleates at the load interface. The transition wave propagating into the chain creates a checkered energy pattern [Fig. 3(a)]. The same phenomenon arises when compressing a chain of disks with two and four embedded magnets [Figs. 3(b) and 3(d)]. In the case of two magnets per disk, the energy pattern is distinctly different from the previous pattern (for one magnet per disk) and the transition wave propagates further down the chain at the same rate of compression as panel (a). However, the transition wave does not reach the end of the chain in either case. At four magnets per disk, the transition wave reaches the end of the chain at ($\approx$0.25 m) compression, significantly changing the emerging energy pattern. In the case of three magnets per disk, the equilibrium positions before deformation have a high-energy state due to the frustration-induced disorder. This state is elucidated by the thin green line at top of Fig. 3(c), which is consistent with our previous experimental observation [Fig. 2(k)]. Surprisingly, the frustration-induced disorder vanishes after applying a small load to the chain. This compression ($\approx$0.01 m) causes all the disks to align perfectly with a minimum energy state [a thin horizontal dark-blue line in Fig. 3(c)]. The self-alignment, or this emergent *deformation-induced order* happens every time the chain is compressed by a full unit cell length (i.e., 0.028 m), appearing as flat blue lines in Fig. 3(c).

To experimentally verify our numerical observations, we consider a chain of ten free-floating disks within the same magnetic boundary (Fig. 2). We apply a load at the leftmost disk, at equilibrium [Figs. 4(a)–4(d)], causing the disk to snap into the next potential well. This nucleates the first defect [highlighted with dashed red boxes in Figs. 4(a)–4(d)]. In the case of three magnets per disk, we experimentally observe the emergent *deformation-induced order*. All the ordered lattices are highlighted green in Figs 4(a)–4(d). As the load increases, the defect migrates further down the chain and a new defect arises [highlighted with dashed orange boxes in Figs. 4(a)–4(d)]. As more defects nucleate, a pattern of alternating defect and defect-free cells emerges. This is congruent with the energy patterns observed numerically (Fig. 3).

We observe different defect topologies depending on the disk type. For disks with one embedded magnet, we identify one defect type as two disks, aligned horizontally, confined within the same potential well [Fig. 4(e)]. In the case of two magnets per disk, we observe two distinct defects with two disks per potential well. The normal to the line connecting the centers of the two defect disks points either left or right [Fig. 4(f)]. In the case of three magnets per disk, we observe a combination of these three defect topologies (i.e., flat, pointing left, or pointing right) [Fig. 4(g)]. In the case of four magnets per disk, the defect is composed of three disks, not two, sharing two adjacent potential wells. There is either a horizontal alignment of the three disks or a mix of left and right pointing normals [Fig. 4(h)].

The deformation-induced pattern transformation displays a distinct topological signature with different disk couplings. This translates to a change in material properties as patterns evolve. We experimentally test the dynamical characteristics of the emerging patterns by exciting three of the newly formed lattices for each of the disk types (Fig. 5). For reference, we first harmonically excite the undeformed self-aligned chain
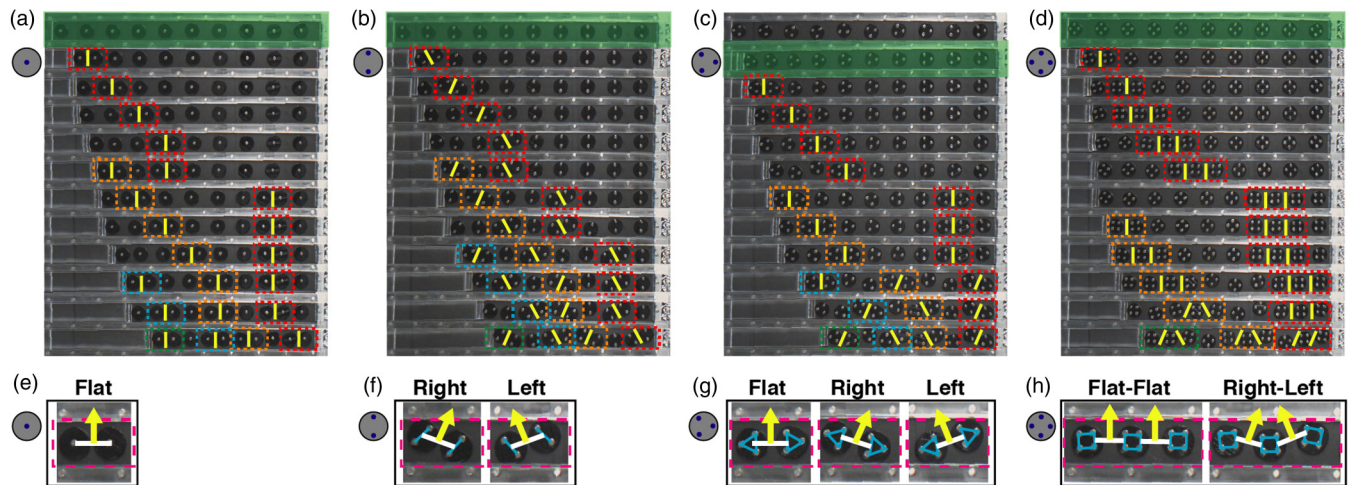
FIG. 4. *(a)–(d) Defect nucleation and propagation.* Stepwise deformation of ten levitated disks with one to four embedded magnets per disk. The defects are marked with the same color dashed box as they propagate through the material. (e)–(h) The different types of defects arising for various disk types. The perfectly aligned state is highlighted with a green solid rectangle [top picture in each panel except for the frustrated state in (c)]. The normals are highlighted in yellow throughout all panels.

of ten magnets with a chirp signal between 0.2 and 35 Hz and record the transmission through the lattice (1D FFT). The leftmost disk is then compressed until a new pattern emerges across the ten disks. The chain is then excited with the same chirp signal. The experiment is repeated for two emerging patterns [panels (ii) and (iii) in Fig. 5] in addition to the pattern of the undeformed disks [panels (i) in Fig. 5]. The basic repeating pattern in each case is also included (Fig. 5 insets).
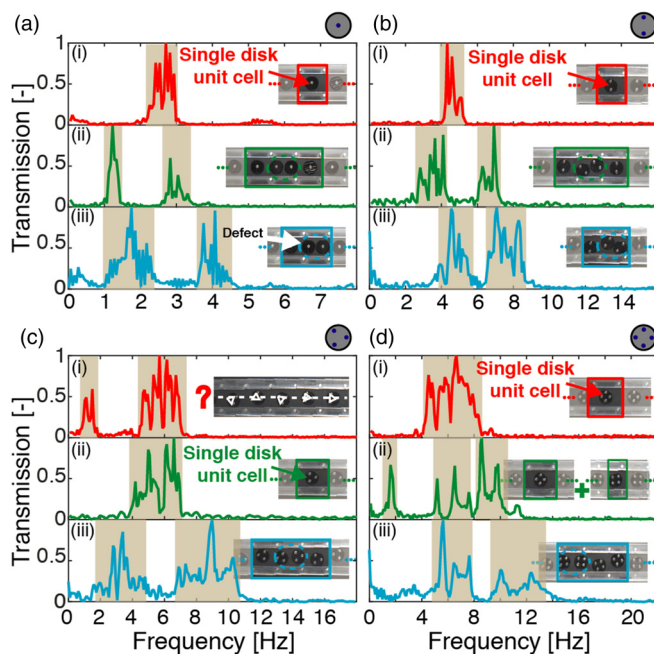

FIG. 5. *Tunable wave propagation.* (a)–(d) Experimentally measured transmission in a lattice with one to four embedded magnets per disk. (i) Transmission through the uncompressed configuration for each disk type. (ii),(iii) Transmission within the lattice after deformation. The insets show the corresponding basic building block in each case.

With the one-magnet per disk arrangement, the reference pattern has a single longitudinal transmission band [Fig. 5(a(i))]. This single band turns into two distinct bands when the pattern is a defect cell sandwiched between two defect-free cells [Fig. 5(a(ii))]. As the load increases and the pattern turns into a single defect-free cell and a defect cell, both bands widen and shift to higher frequencies [Fig. 5(a(iii))]. The same phenomenon takes place for disks with two embedded magnets. The reference assembly with perfectly aligned disks transitions into a defect sandwiched between two defect-free cells. The pattern then transforms into a single defect-free and a defect cell, with the emergence of two wider transmission bands at higher frequencies [Figs. 5(b(i))–5(b(iii))]. In the three magnets per disk case, the initial pattern is frustrated with no long-range order. As observed earlier [Fig. 2(g)], two transmission bands are present [Fig. 5(c(i))]. Once the lattice is compressed, the deformation-induced order emerges and the low-frequency disorder-induced band disappears [Fig. 5(c(ii))]. As the load increases, the pattern transforms further into a defect cell sandwiched between two defect-free cells [Fig. 5(c(iii))]. Finally, at four magnets per disk, the lattice transforms from aligned disks in a 0° phase angle into two neighboring lattices with 0° and 45° phase angles [Fig. 5(d(ii))]. The difference in transformation for this disk type is a combination of both the number of disks within the defect (i.e., three instead of two) and the small number of disks considered in the experiment (i.e., only ten disks). As the load increases, two transmission bands emerge as the pattern transforms into an alternation of two defect-free cells and one defect cell [Fig. 5(d(iii))].

In summary, we consider free-floating magnetic disks within a magnetic boundary with periodic potentials. The levitated disks perfectly align in the case of one, two, and four magnets per disk. In the case of three magnets per disk, the global lattice assembly shows no long-range order due to the presence of geometric frustration. Despite the clear disorder, the transmission within the lattice closely resembles that of a perfectly ordered lattice. For all different disk types, we

further transform the self-alignment of the disks by applying a load at one end of each emerging lattice. We observe the nucleation and propagation of different defect types (depending on the number of magnets per disk) within the lattices, giving rise to *time-independent* stable transition waves due to instabilities. Remarkably, in the presence of frustration (i.e., three magnets per disk), the applied load briefly introduces a stable order to the assembly. By further deforming the lattices, new patterns emerge across all disk types. We harness these emerging patterns to tune the harmonic wave propagation characteristics of the soft material. Our findings shed light on the understanding of deformation-induced pattern transformations, particularly the rise of frustration-induced disorder and deformation-induced order. The nature of the localized and stable defect propagation, in addition to the nonlinear coupling potentials, can be harnessed in designing the next generation of soft materials for applications ranging from sound manipulation to soft robotics.

[1] E. Norouzi, A. A. Watkins, and O. R. Bilal, Phys. Rev. E **104**, 044902 (2021).

[2] S. M. Taheri, M. Michaelis, T. Friedrich, B. Förster, M. Drechsler, F. M. Römer, P. Bösecke, T. Narayanan, B. Weber, I. Rehberg *et al.*, Proc. Natl. Acad. Sci. USA **112**, 14484 (2015).

[3] P. Mellado, A. Concha, and L. Mahadevan, Phys. Rev. Lett. **109**, 257203 (2012).

[4] J. Schönke, T. M. Schneider, and I. Rehberg, Phys. Rev. B **91**, 020410(R) (2015).

[5] P. Wang, Y. Zheng, M. C. Fernandes, Y. Sun, K. Xu, S. Sun, S. H. Kang, V. Tournat, and K. Bertoldi, Phys. Rev. Lett. **118**, 084302 (2017).

[6] S. H. Kang, S. Shan, A. Košmrlj, W. L. Noorduin, S. Shian, J. C. Weaver, D. R. Clarke, and K. Bertoldi, Phys. Rev. Lett. **112**, 098701 (2014).

[7] H. T. Diep, ed., *Frustrated Spin Systems* (World Scientific, Singapore, 2013).

[8] D. M. Kochmann and K. Bertoldi, Appl. Mech. Rev. **69**, 050801 (2017).

[9] J. Li, T. D. Pallicity, V. Slesarenko, A. Goshkoderia, and S. Rudykh, Adv. Mater. **31**, 1807309 (2019).

[10] A. Goshkoderia, V. Chen, J. Li, A. Juhl, P. Buskohl, and S. Rudykh, Phys. Rev. Lett. **124**, 158002 (2020).

[11] L. Jin, R. Khajehtourian, J. Mueller, A. Rafsanjani, V. Tournat, K. Bertoldi, and D. M. Kochmann, Proc. Natl. Acad. Sci. USA **117**, 2319 (2020).

[12] B. Haghpanah, L. Salari-Sharif, P. Pourrajab, J. Hopkins, and L. Valdevit, Adv. Mater. **28**, 7915 (2016).

[13] B. Florijn, C. Coulais, and M. van Hecke, Phys. Rev. Lett. **113**, 175503 (2014).

[14] B. Florijn, C. Coulais, and M. van Hecke, Soft Matter **12**, 8736 (2016).

[15] O. B. Matar, J. Vasseur, and P. A. Deymier, in *Acoustic Metamaterials and Phononic Crystals* (Springer, New York, 2013), pp. 253–280.

[16] O. R. Bilal, A. Foehr, and C. Daraio, Proc. Natl. Acad. Sci. USA **114**, 4603 (2017).

[17] O. R. Bilal, A. Foehr, and C. Daraio, Adv. Mater. **29**, 1700628 (2017).

[18] A. Palermo, Y. Wang, P. Celli, and C. Daraio, Phys. Rev. Appl. **11**, 044057 (2019).

[19] Y. Wang, B. Yousefzadeh, H. Chen, H. Nassar, G. Huang, and C. Daraio, Phys. Rev. Lett. **121**, 194301 (2018).

[20] Y.-F. Wang, Y.-Z. Wang, B. Wu, W. Chen, and Y.-S. Wang, Appl. Mech. Rev. **72**, 040801 (2020).

[21] T. Chen, O. R. Bilal, K. Shea, and C. Daraio, Proc. Natl. Acad. Sci. USA **115**, 5698 (2018).

[22] P. Rothemund, A. Ainla, L. Belding, D. J. Preston, S. Kurihara, Z. Suo, and G. M. Whitesides, Sci. Rob. **3**, eaar7986 (2018).

[23] A. Zareei, B. Deng, and K. Bertoldi, Proc. Natl. Acad. Sci. USA **117**, 4015 (2020).

[24] K. Bertoldi and M. C. Boyce, Phys. Rev. B **78**, 184107 (2008).

[25] P. Wang, J. Shim, and K. Bertoldi, Phys. Rev. B **88**, 014304 (2013).

[26] S. Shan, S. H. Kang, P. Wang, C. Qu, S. Shian, E. R. Chen, and K. Bertoldi, Adv. Funct. Mater. **24**, 4935 (2014).

[27] J. Shim, P. Wang, and K. Bertoldi, Int. J. Solids Struct. **58**, 52 (2015).

[28] J. R. Raney, N. Nadkarni, C. Daraio, D. M. Kochmann, J. A. Lewis, and K. Bertoldi, Proc. Natl. Acad. Sci. USA **113**, 9722 (2016).

[29] J. Li, J. Shim, J. Deng, J. T. Overvelde, X. Zhu, K. Bertoldi, and S. Yang, Soft Matter **8**, 10322 (2012).

[30] See Supplemental Material at http://link.aps.org/supplemental/10.1103/PhysRevB.104.L140101 for details about energy calculations, experimental methods, numerical details and dispersion analysis.

[31] A. A. Watkins and O. R. Bilal, Front. Mater. **7**, 410 (2020).

[32] W. Jiao and S. Gonella, Phys. Rev. B **102**, 054304 (2020).

[33] W. H. Press, S. A. Teukolsky, W. T. Vetterling, and B. P. Flannery, *Numerical Recipes: The Art of Sscientific Computing*, 3rd ed. (Cambridge University Press, Cambridge, UK, 2007).

[34] N. Boechler, J. Yang, G. Theocharis, P. Kevrekidis, and C. Daraio, J. Appl. Phys. **109**, 074906 (2011).

[35] P. Wang, F. Casadei, S. Shan, J. C. Weaver, and K. Bertoldi, Phys. Rev. Lett. **113**, 014301 (2014).

[36] S. Babaee, N. Viard, P. Wang, N. X. Fang, and K. Bertoldi, Adv. Mater. **28**, 1631 (2016).

[37] A. Amendola, A. Krushynska, C. Daraio, N. M. Pugno, and F. Fraternali, Int. J. Solids Struct. **155**, 47 (2018).